

Micro-Abrasion Wear Resistance of Borided 316L Stainless Steel and AISI 1018 Steel

C.D. Reséndiz-Calderon, G.A. Rodríguez-Castro, A. Meneses-Amador, I.E. Campos-Silva, J. Andraca-Adame, M.E. Palomar-Pardavé, and E.A. Gallardo-Hernández

(Submitted January 31, 2017; in revised form June 24, 2017)

The 316L stainless steel has high corrosion resistance but low tribological performance. In different industrial sectors (biomedical, chemical, petrochemical, and nuclear engineering), improvement upon wear resistance of 316L stainless steel components using accessible and inexpensive methods is critical. The AISI 1018 steel is widely used in industry, but its tribological performance is not the best among steels. Therefore, in this study the behavior of the borided 316L stainless steel and 1018 steel is evaluated under micro-abrasion wear. The boriding was carried out at 1223 K over 6 h of exposure time, resulting in a biphasic layer composed of FeB/Fe₂B phases. In order to evaluate Fe₂B phase with no influence from FeB phase, AISI 1018 steel samples were borided at 1273 K for over 20 min and then diffusion annealed at 1273 K over 2 h to obtain a Fe₂B mono-phase layer. Micro-abrasion wear resistance was evaluated by a commercial micro-abrasion testing rig using a mix of F-1200 SiC particles with deionized water as abrasive slurry. The obtained wear rates for FeB and Fe₂B phases and for the 316L stainless steel were compared. Wear resistance of 316L stainless steel increases after boriding. The wear mechanisms for both phases and for the stainless steel were identified. Also, transient conditions for rolling and grooving abrasion were determined for the FeB and Fe₂B phases.

Keywords boriding, FeB, Fe₂B, micro-abrasion, wear resistance, wear mode maps

1. Introduction

AISI 316L stainless steel is extensively used in various areas of industry such as the biomedical, chemical, petrochemical, and nuclear engineering because of its high corrosion resistance even at high temperatures. However, its defective tribological performance represents a restriction when it needs to be used on applications that involve sliding against other materials (Ref 1). In such situations, where other properties such as its abrasion resistance become important, a surface modification technique could be useful. The boriding process offers a good chance to overcome this obstacle by enhancing its mechanical properties. Different investigations have demonstrated that on this steel, boriding is able to increase its surface hardness and maintain

acceptable corrosion resistance and can even increase it in particular environments (Ref 2-4).

The powder-pack boriding process is a diffusion treatment which is capable of improving hardness, wear, and corrosion resistance of a variety of ferrous and non-ferrous metals. When it is applied on steels, it forms iron boride layers which can be formed by two phases (FeB/Fe₂B) or just one phase (FeB) depending on the boron potential on the external surface of the steel, the temperature process, and the exposure time. Mechanical properties of both phases depend on the chemical composition of the borided steel, although commonly the hardness of FeB phase is higher than the Fe₂B phase. On the other hand, fracture toughness is higher for the Fe₂B phase (Ref 5).

The growth kinetics of borided stainless steels has been studied by some researchers using mathematical models based on the mass balance at the growing interfaces (Ref 6-10). The process begins with the nucleation of borides on the material surface and continues with a columnar growth as a consequence of the diffusion of boron perpendicular to the surface. Campos-Silva et al. (Ref 6) and Kedamm (Ref 7) presented a diffusion model to estimate the kinetic of a FeB/Fe₂B layer and its diffusion zone on the surface of a 316L stainless steel exposed to the boriding treatment. A parabolic growth law described by $d^2 = k(t - t_0)$ where d represents thickness, t the exposure time, t_0 the incubation time, and k the rate growth constant depending on temperature process was considered. According to their experimental results, when a two-phase layer (FeB/Fe₂B) is formed, the Fe₂B phase grows for a certain time before the formation of the FeB phase. Activation energies were determined for the formation of FeB and Fe₂B phases. Hence, Ozdemir et al. (Ref 10) calculated the kinetic rates for borided 316L stainless steel by using Arrhenius equation; the activation energy of boride growth for this study was determined as 199 kJ/mol.

C.D. Reséndiz-Calderon, G.A. Rodríguez-Castro, A. Meneses-Amador, and I.E. Campos-Silva, Instituto Politécnico Nacional, Grupo Ingeniería de Superficies, SEPI-ESIME, U.P. Adolfo López Mateos, Zacatenco, 07738 Ciudad de México, Mexico; J. Andraca-Adame, Instituto Politécnico Nacional, Centro de Nanociencias y Micro y Nanotecnologías, U.P. Adolfo López Mateos, Zacatenco, 07738 Ciudad de México, Mexico; M.E. Palomar-Pardavé, Universidad Autónoma Metropolitana, Av. San Pablo No. 180, Azcapotzalco, 02200 Ciudad de México, México; and E.A. Gallardo-Hernández, Instituto Politécnico Nacional, Grupo de Tribología, SEPI-ESIME, U.P. Adolfo López Mateos, Zacatenco, 07738 Ciudad de México, México. Contact e-mail: garodriguezc@ipn.mx.

However, research on the wear resistance of borided AISI 316L stainless steel is limited (Ref 4) and focused on sliding wear, while works on wear resistance of similar coatings only include adhesive wear and two-body abrasive wear (Ref 11-13), disregarding situations in which a third body could be the cause of wear. Martini et al. (Ref 14) evaluated abrasive wear resistance of a FeB/Fe₂B coating formed on Armco iron and a low-carbon steel by micro-abrasion testing but only obtained specific wear rates for different sliding distances and with no distinctions of the wear resistance of each phase. Gunes and Yildiz (Ref 15) evaluated the adhesion and tribological behavior (ball-on-disk configuration) of FeB/Fe₂B formed on borided 310 stainless steel; they found sufficient adhesion strength and a reduction of the COF with respect to the non-boriding 310 stainless steel. Günen et al. (Ref 16) used the micro-abrasion test to assess the abrasion resistance of a FeB/Fe₂B coating on a AISI 304 stainless steel, but the images shown in his work only reveal two-body abrasion wear mechanisms and do not determine wear constants of individual phases or the complete coating. The nearest precedent of this research is a previous work of the authors about the micro-abrasion resistance of a boride coating formed on a CoCrMo alloy (Ref 17).

The micro-abrasion test is not a standardized wear test, but there are a significant amount of investigations supporting its effectiveness, reproducibility, and its main sources of variability (Ref 18-22), making it an attractive and useful wear evaluation method. The small resulting scars of the test allow it to be applied in small volumes and avoid mechanical influences of substrate in the coatings evaluation.

Therefore, the objective of this work is to determine the third-body abrasion (rolling abrasion) wear performance of FeB phase present on a borided stainless steel by means of the micro-abrasion test. To evaluate the performance of the internal Fe₂B phase, the employment of the mono-phase layer (Fe₂B) formed on an AISI 1018 steel was proposed, in order to avoid a penetration test on the borided AISI 316L stainless steel. This is because the morphology of the borided AISI 316L stainless steel coating is not completely plane and this condition could be Fe₂B. Additionally, wear resistance of iron borides and that of substrate are compared. The transient conditions between rolling abrasion and grooving abrasion wear mechanisms for both phases and the stainless steel are obtained and outlined by a wear mode map.

2. Experiment Details

2.1 Boriding Process

Both AISI 316L stainless steel and AISI 1018 low-carbon steel with a nominal composition of 17-20 wt.% Cr, 12-14 wt.

% Ni, 2-4% wt.% Mo, and 0.03 wt.% C for the former and 0.15-0.2 wt.% C, 0.6-0.9 wt.% Mn, 0.04 wt.% max P, and 0.05 wt.% max S for the latter were employed. Circular-shaped samples of 4 mm of thickness were sectioned from a cylindrical bar of 25.4 mm of diameter for both materials. Prior to the boriding process, all specimens were polished and ultrasonically cleaned with isopropyl alcohol for 15 min at room temperature and dried and stored under a clean room conditions. Subsequently, samples were embedded in a closed cylindrical case (AISI 304) containing Ekabor 2 powder mixture as a boron-rich agent.

For the AISI 316L stainless steel, the boriding treatment was performed at a temperature of 1223 K and 6 h of exposure time, while for the AISI 1018 low-carbon steel the processing temperature was 1273 K and 20 min of exposure time. Once the treatment time was completed, the container was removed from the electrical furnace and slowly cooled to room temperature. Samples borided AISI 1018 low-carbon steel additionally underwent a diffusion annealing treatment in order to obtain a mono-phase coating consisting of Fe₂B. These samples were embedded in a closed cylindrical case with F-1200 SiC powder acting as a diluent (Ref 23). The container was heated at a temperature of 1273 K for 2 h and then cooled in air.

Borided samples were then cross-sectioned for metallographic preparation and etched with Vilella's reagent in the case of the borided AISI 316L stainless steel and 2% nital solution for borided plus diffusion-annealed AISI 1018 low-carbon steel for their characterizations using GX51 Olympus equipment. Bragg-Brentano geometry for x-ray diffraction was used in PANalytical X'Pert Pro MRD diffractometer for the identification of phases. Measurements were taken with Co K α ($\lambda = 1.79 \text{ \AA}$) radiation as a source with linear focus and 45 kV and 40 mA. For the incident optics, parallel beam x-ray lens and the PIXcel detector (2.5°) were used. X-ray patterns were obtained from 43° to 105° with 0.05° by step, and time per angular step was 300 s. Also XRD patterns were exported from HighScore Plus software from PANalytical.

2.2 Mechanical Properties

Resulting coating on the borided AISI 316L stainless steel, borided AISI 1018 steel and the borided plus diffusion-annealed AISI 1018 low-carbon steel were characterized on a commercial nanoindenter CSM Indentation Tester (TTX-NHT) with a Berkovich diamond tip following the recommendations of the ISO 14577 standard (Ref 24). Hardness and Young's modulus profiles were obtained. The indentations were carried out in a cross section of the FeB/Fe₂B biphasic and Fe₂B mono-phase coatings at different distances from the surface using a constant load of 25 mN. At least three indentations were performed for each distance from the surface with load/unload rates of 50 mN/min and a dwell time of 10 s. The load-

Table 1 Experimental parameters for wear rate evaluation and for wear mode maps

Experimental parameter	Wear rate	Wear mode maps
Applied load	0.2 N	0.2, 0.5, 1, 1.5, and 2 N
Abrasive volume concentration	20% (80 g/100 ml)	5, 10, 15, and 20%
Sliding distance	16, 32, 48, 64, and 80 m	5 m for FeB and Fe ₂ B 15 m for AISI 316L stainless steel
Rotational speed	0.1 m/s	0.1 m/s
Counterface material	AISI 52100	AISI 52100
Counterface dimensions	Diameter 25.4 mm	Diameter 25.4 mm

displacement curves were analyzed according to the Oliver–Pharr procedure, which consider the projected area of the Berkovich indenter and the contact depth of indentation (Ref 25). The Poisson’s ratio was set to 0.25. The Young’s modulus was determined from slope of the unloading curve at maximum load. The Young’s modulus is a function of dP/dh and the contact area as shows Eq 1.

$$E = \frac{1}{2} \frac{\sqrt{\pi} dP}{A dh} \quad (\text{Eq 1})$$

In addition, the hardness was determined from indentation load divided by the projected contact area ($H = P/A$).

2.3 Micro-Abrasion Test

Rolling abrasion or three-body abrasion tests were performed on a Phoenix Tribology Plint Te-66 micro-abrasion rig for the FeB, Fe₂B and AISI 316L stainless steel wear resistance evaluation. In this test, a driven ball is rotated against a flat specimen, which is mounted on a dead-weight load lever, in the presence of abrasive slurry. The slurry is drip-fed onto the contact point between the specimen and the ball, and the wear scar produced on the specimen surface is assumed to reproduce the spherical geometry of the ball. AISI 52100 steel balls with 25.4 mm of diameter were used as a counterface in the tests. To augment the reproducibility, the balls were prepared superficially by etching (mixture of nitric acid and ethyl alcohol with 30% and 70%, respectively) to obtain a roughness of $R_a = 0.40 \mu\text{m}$ (Ref 19-21). All balls were used no more of four times and were rotated at the end of each test. To avoid effects of abrasive particle size, shape, and hardness and also ensure the repeatability of micro-abrasion tests, an abrasive slurry consisting of F-1200 SiC particles (4-5 μm) dissolved in a 20% volume proportion (80gr/100 ml) with deionized water was selected. To prevent setting of SiC particles, the abrasive slurry was constantly agitated with the aid of a magnetic stirrer. Each test was repeated three times.

Borided AISI 316L stainless steel was used to evaluate the wear constant of the FeB phase, taking care to never penetrate the Fe₂B phase. The borided plus diffusion-annealed AISI 1018 low-carbon steel was used to determine the wear constant of the Fe₂B phase. It would be important to point out that even when the chemical composition of the Fe₂B formed on AISI 316L stainless steel and Fe₂B formed on the borided plus diffusion-annealed AISI 1018 low-carbon steel is different, both phases have a tetragonal crystalline structure with a boron content of approximately 8.9 wt.%. Scar wears never reached the substrate on these specimens. Finally, the received AISI 316L stainless steel was also evaluated to compare the results of micro-abrasion wear resistance of iron borides.

Since in the tests there are never two different phases carrying the wear, it is possible to consider them as bulk material tests. The volume of wear scars (V) was calculated by optical profilometer. Archard’s equation (Eq 2) was used to estimate the wear constant (Ref 21):

$$V = kSN \quad (\text{Eq 2})$$

where S represents the relative wear distance, N is the applied load, and k is the wear constant of the material also known as the wear rate. The wear craters were measured

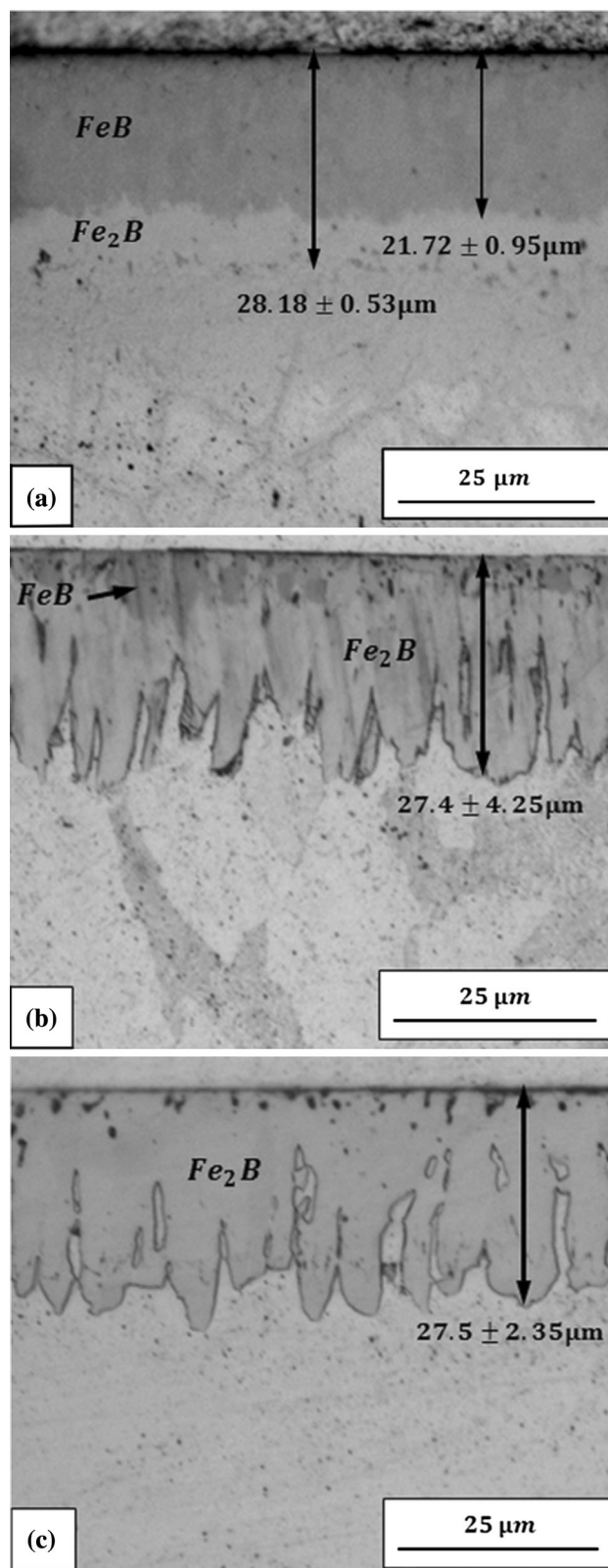


Fig. 1 Cross-sectional view of the coatings after on (a) AISI 316L stainless steel, 1223 K and 6 h, (b) AISI 1018 low-carbon steel, 1273 K and 20 min. (c) Borided plus diffusion-annealed AISI 1018 low-carbon steel, 1273 K and 2 h

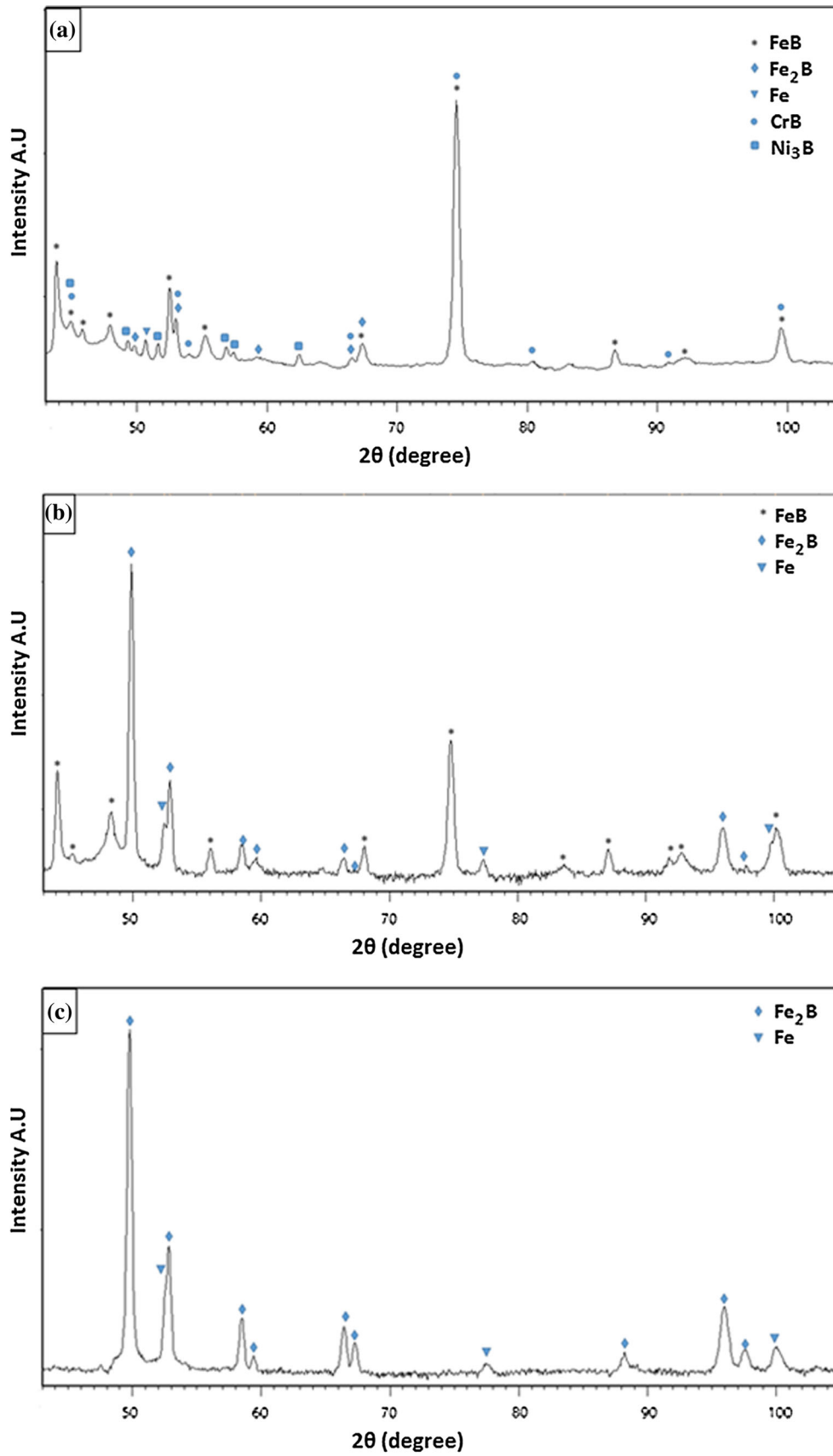


Fig. 2 X-ray diffraction pattern obtained for (a) boriding AISI 316L stainless steel, (b) boriding AISI 1018 steel, (c) borided plus diffusion-annealed AISI 1018 steel

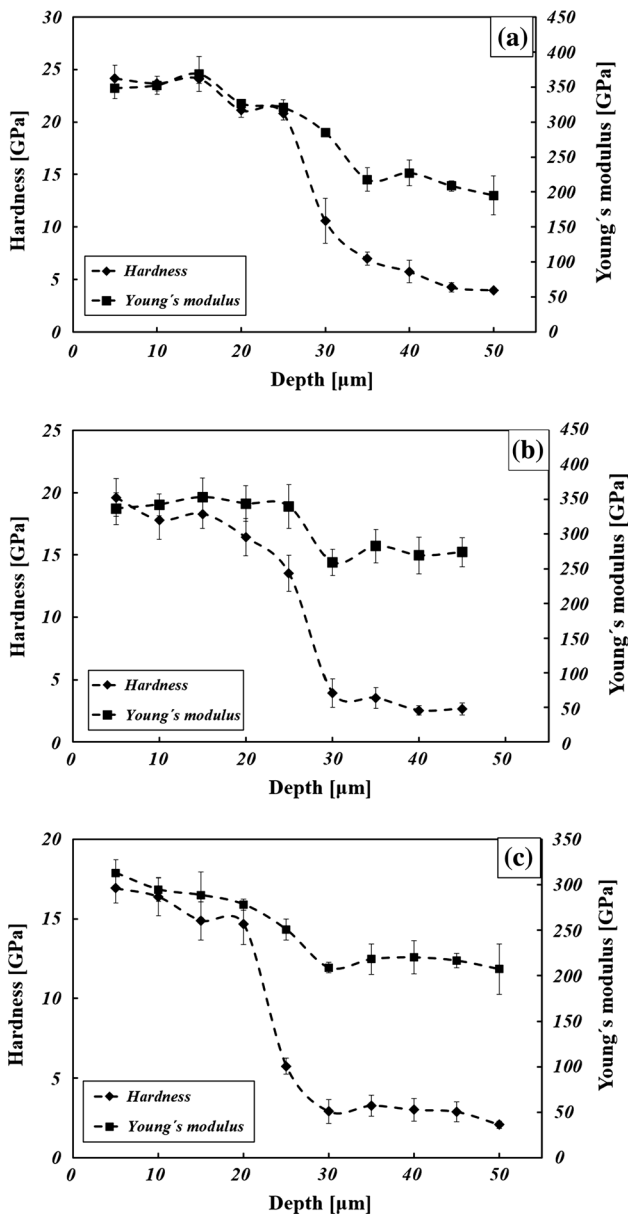


Fig. 3 Hardness and Young's modulus profile obtained in the cross section of (a) borided AISI 316L stainless steel, (b) borided AISI 1018 steel, (c) borided plus diffusion-annealed AISI 1018 steel

using a GX51 Olympus optical microscope. Additionally, a cross section of the resulting wear scars was evaluated by using an optical profilometer (Contour GT-K, Bruker).

Transient conditions for rolling (three-body abrasion) and grooving (two-body abrasion) were determined for the FeB and Fe₂B phases. A wear mode map for the AISI 316L stainless steel was also generated. For these tests, caution was taken to prevent penetration of one phase to another or from the coating to the substrate during each test. Sliding distance was kept constant for FeB and Fe₂B coatings (5 m) and for the stainless steel (15 m). The applied load and volume concentration of SiC particles in the slurry were the variable parameters. Each test condition was repeated three times. Table 1 summarizes test conditions for both wear rate evaluation and wear mode map obtainment.

3. Results

3.1 Boriding Process

A flat morphology tendency was observed with an optical microscope on the surface of the borided stainless steel with a biphasic FeB/Fe₂B coating (Fig. 1a). Total thickness and the FeB phase thickness are $28.18 \pm 0.53 \mu\text{m}$ and $21.72 \pm 0.95 \mu\text{m}$, respectively. An essentially Fe₂B mono-phase coating with the presence of some crystals from the FeB phase near the surface was observed by optical microscopy on the borided AISI 1018 low-carbon steel (Fig. 1b). This coating exhibits a saw-toothed morphology with a total thickness of $27.4 \pm 4.25 \mu\text{m}$ and a small zone of the FeB phase of approximately $5 \mu\text{m}$. After diffusion annealing process was applied to the borided AISI 1018 steel, a complete mono-phase coating of Fe₂B is shown in Fig. 1(c). Borided plus diffusion-annealed low-carbon steel remained with a saw-toothed morphology, but its thickness slightly grew (Ref 23); the resulting thickness of this coating is $27.50 \pm 2.35 \mu\text{m}$. Moreover, XRD patterns (Fig. 2a) reveal the presence of FeB, Fe₂B, CrB, and Ni₃B for borided 316L steel. For borided 1018 steel are identified FeB and Fe₂B (Fig. 2b), but for borided plus diffusion-annealed 1018 steel only Fe₂B phase is presented (Fig. 2c). Additionally, iron is detected in the three borided steels.

3.2 Mechanical Properties

The estimated hardness and Young's modulus values from the instrumented indentation with a Berkovich tip are shown in Fig. 3. At the FeB/Fe₂B coating formed on the AISI 316L stainless steel, the maximum hardness and Young's modulus values of 24 and 350 GPa, respectively, are reached near the surface where the FeB phase is present. Both hardness and Young's modulus decrease in magnitude as they are nearer to the surface. Fe₂B is not as hard as the FeB phase but is still harder than the stainless steel with a hardness of 21 GPa and Young's modulus of 320 GPa. At the diffusion zone, hardness and Young's modulus reach values of 10 and 285 GPa. Finally, the substrate possesses the lowest hardness and Young's modulus values with 4.5 and 210 GPa, respectively. For borided AISI 1018 steel, the hardness and Young's modulus reached values of 19 and 340 GPa for the FeB phase, while for the Fe₂B phase 18 and 320 GPa, respectively. For borided plus diffusion-annealed AISI 1018, the average hardness of the Fe₂B phase is 16 GPa, while its Young's modulus reaches 290 GPa.

3.3 Micro-Abrasion Test

Figure 4 show the wear craters obtained on the FeB phase for the studied sliding distances. All figures reveal rolling abrasion wear as the main wear mechanism. Wear craters for the Fe₂B phase and for AISI 316L steel also have rolling abrasion wear, only changing the diameter and depth of the wear craters according to the abrasive resistance of each one. To determine their wear rates, wear volumes were plotted as a function of applied load (0.2 N) and wear sliding distance for the three different materials (Fig. 5). The slope of the resulting linear plot for each material is the wear rate according to Eq 1. Wear rates were obtained through each individual slope by a square-minimum linear fit with a correlation factor of $R^2 > 0.99$. Table 2 summarizes wear rate results. According to Table 2, the FeB phase has the highest wear abrasion resistance

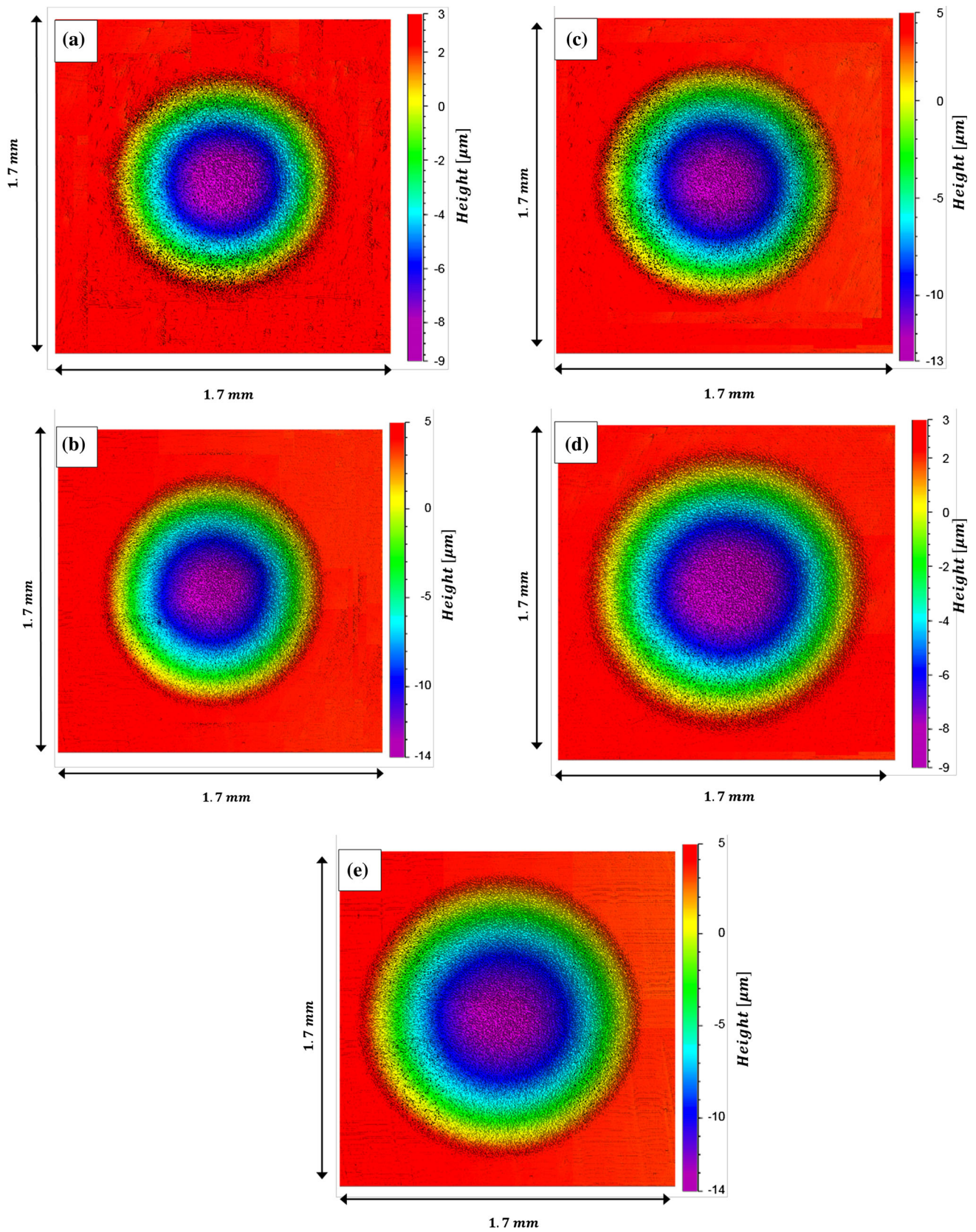


Fig. 4 Wear scars observed by optical profilometry on FeB phase (borided 316L stainless steel) for (a) 16 m, (b) 32, (c) 48 m, (d) 64 m, and (e) 80 m

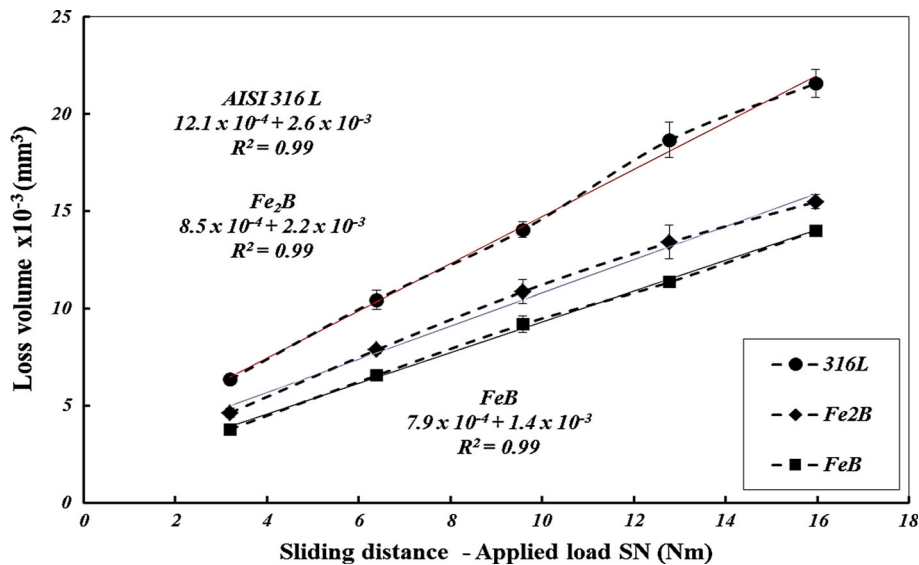


Fig. 5 Linear plots to obtain wear rates for FeB phase, Fe₂B phase, and AISI 316L stainless steel

Table 2 Wear rates of AISI 316L stainless steel and iron borides

	FeB	Fe ₂ B	AISI 316L
$K(\times 10^{-4}) \text{ mm}^3/\text{Nm}$	7.9 ± 0.21	8.5 ± 0.46	12.1 ± 0.07

followed by the Fe₂B phase. The AISI 316L stainless steel has the maximum value of wear rate, which indicates that it loses a greater amount of volume for each newton meter applied.

Figure 6 shows transient conditions for rolling and grooving abrasion mechanisms at the FeB and Fe₂B phases. As mechanical properties of these phases are similar, wear mode maps have only small differences among them. On both cases, rolling abrasion is present when abrasive particle concentrations in the slurry are high and the applied load is low, while grooving abrasion appears when the applied load is increased and abrasive particle concentrations decrease. Figure 7 shows the wear mode map of the AISI 316L stainless steel distinguishing three different zones. The rolling abrasion zone is present when the applied loads are low and abrasive particle concentrations are high. Next to the rolling abrasion zone is the transition zone or the mix mode zone. The grooving abrasion mechanism is not present on this map; instead of it, Ridge's effect appears.

4. Discussions

These types of morphology produced in AISI 316L stainless steel and 1018 can be explained by their alloying elements. The Cr, Ni, and Mo inhibit the growth of the layer; they reduce the activated boron flux in the tips of boride columns and reduce the columnar shape in comparison with AISI 1018 steel, where the columnar nature of coating interface is attributed to the increase in growth due to the fields of local high stress and lattice distortions (Ref 26). The increase in the layer thickness and FeB phase dissolution of borided plus diffusion-annealed

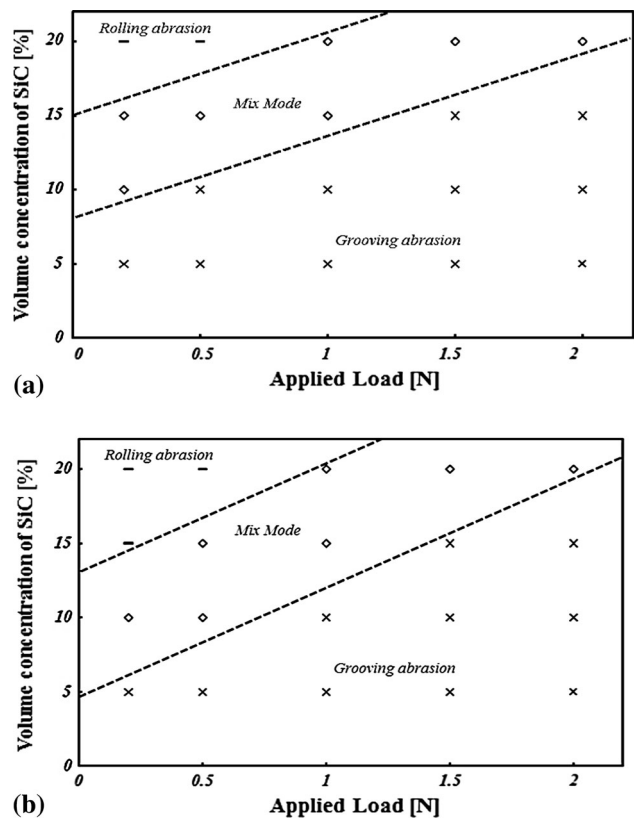


Fig. 6 Transient conditions for rolling and grooving abrasion mechanisms for (a) FeB phase and (b) Fe₂B phase

AISI 1018 steel are due to the boron concentration gradient; boron diffuses from the FeB phase along the grain boundaries through the steel (Ref 23). Elemental analysis by energy-dispersive x-ray (EDS) was performed in JEOL JSM Scanning Electron Microscopy—model 7800 (Fig. 8). For AISI 316L steel (Fig. 8a) around 21 μm, a decrease in the boron intensity that is related to the phase change from FeB to Fe₂B is

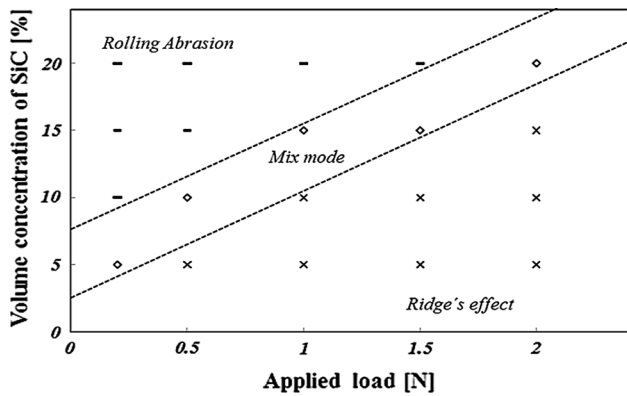


Fig. 7 Transient conditions for rolling abrasion mechanism and Ridge's effect for the AISI 316L stainless steel

observed. Moreover, alloy elements (Cr, Ni, Mo) dissolved in the borides layer are identified. The Cr has an atomic number smaller than the iron facilitating its insertion in the layer of borides. But the Ni atomic number is greater than the iron, and its insertion is more difficult in the boron layer (Ref 27). However, most of these elements are accumulated in the diffusion zone below the Fe_2B phase formed a zone rich in Ni and Cr formed by a thin layer and Cr precipitation in the grain boundaries (Ref 28); in fact, the FeB phase generally contains high boron products dissolved therein and is known as FeB-base phase (Ref 29). In the borided AISI 1018 steel, the manganese is typically used to reduce the boride layer thickness and to flatten the saw-tooth morphology. In Fig. 8(c), there is a decrease in the intensity of the boron peak within the first 5 μm after diffusion annealing in the AISI 1018 steel in comparison with borided AISI 1018 steel (Fig. 8b); FeB crystals were dissolved as a consequence of the boron concentration, and boron accumulation is observed below the Fe_2B phase. Presence of porosity near the surface is a consequence of FeB dissolution. This fact can be noticed especially on the minor difference between the thicknesses of peaks along the coating, reducing the standard deviation.

The hardness of borides layer is dependent on the treatment time and temperature of boriding, but the alloy elements play an important role in its value. The hardness of the boride layer reaches high values in steels with alloy elements such as Cr, V, W, and Mo. Hence, the FeB phase formed in AISI 316 steel has hardness values around 24 GPa, but the FeB phase formed in low-carbon steel only reaches values of 19 GPa, showing the effect of the alloy elements on the stainless steel. The stoichiometric characteristic of the borides phases with constant boron concentration causes the hardness profiles to decrease as the indentations are closer to the substrate (Ref 9, 22). At the diffusion zone, hardness and Young's modulus are higher values for borided stainless steel due to the fact that there are some iron borides precipitation products with no coalescence and Cr-rich and Ni-rich compounds.

The formation of the FeB phase on the surface of the AISI 316L stainless steel represents an increase in its micro-abrasion wear resistance of 34%; regarding the Fe_2B phase, the increase is approximately 29%. The rate of material loss experienced by abrasive wear is in direct proportion to the degree of indentation or penetration achieved by the abrasive particles on the surface of the material. In turn, the degree of penetration

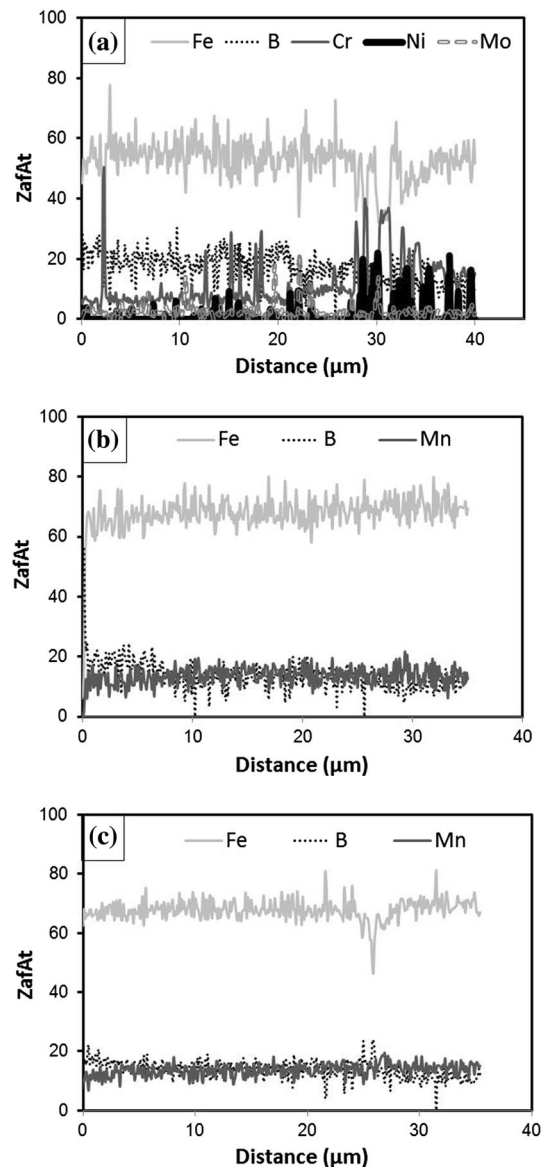


Fig. 8 The EDS line analysis of (a) borided AISI 316L stainless steel, (b) borided AISI 1018 steel, (c) borided plus diffusion-annealed AISI 1018 steel

is strongly influenced by the hardness of the surfaces in contact and the hardness and geometry of the abrasive particles. Figure 9 shows the cross-sectional profile of the wear scars obtained by the micro-abrasion test for AISI 316L stainless steel (Fig. 9a), FeB formed on AISI 316L (Fig. 9b), and Fe_2B formed on AISI 1018 steel (Fig. 9c). High hardness of FeB and Fe_2B phases hinders the penetration of abrasive particles reducing the rate of material loss. Maximum penetration of the stainless steel was reached at 23.24 μm with 4.5 GPa of hardness, while the FeB phase suffered lower penetration values due to high hardness (24 GPa). Wear scars never overtake depths higher than 20 μm for FeB and Fe_2B tests, so the evaluation is always maintained in each of the phases studied. The penetration increases according to the sliding distance.

The rolling abrasion is shown in Fig. 4. This mechanism is produced by multiple indentations of the particles in the

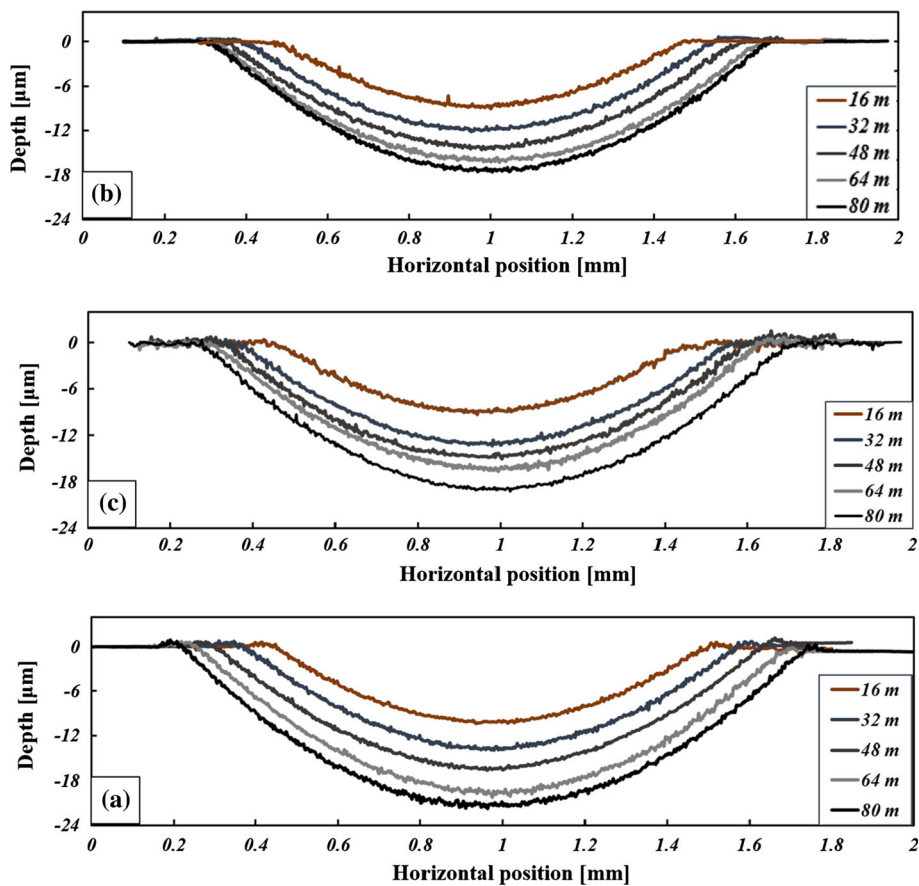


Fig. 9 Cross-sectional profile of micro-abrasion wear scar for (a) AISI 316 L stainless steel, (b) FeB phase formed on AISI 316L stainless steel, (c) Fe₂B phase formed in AISI 1018 steel

sample. It is easily identifiable since there is no pattern in the damage produced. Mechanical properties of the Fe₂B phase formed on AISI 316L stainless steel and the Fe₂B phase obtained on the borided plus diffusion-annealed AISI 1018 steel are not the same. While the Fe₂B phase on the AISI 316L stainless steel reaches hardness values of 21 GPa, the average hardness of the Fe₂B phase on the AISI 1018 is just 16 GPa. The difference in hardness between both phases is caused by the presence of the alloying elements, as has already been mentioned. Therefore, wear rate of these phases (Table 2) must not be the same but must be similar to slightly lower values in the Fe₂B phase present in the borided AISI 316L stainless steel, which was not evaluated due to its non-flat interface with the FeB phase that prevented the formation of a well-defined wear scar.

Results obtained in this work can be compared with those obtained by Rodriguez-Castro et al. (Ref 20) who evaluated micro-abrasion wear resistance of a borided CoCrMo alloy obtaining a wear rate of $K_{CoB} = 7.6 \times 10^{-4} \text{ mm}^3/\text{Nm}$ for the CoB phase. Considering that the CoB phase hardness is 27 GPa and the FeB phase hardness was estimated as 24 GPa, it could be expected that wear rates for these two phases were close. The difference among the wear rates for the CoB phase and the FeB phase obtained in this work is just around 4%. As opposed to the results obtained by Martini et al. (Ref 14) who determined a minor wear resistance of the FeB phase compared to the Fe₂B phase formed on Armco iron and on medium-carbon steel, a better performance of the FeB phase was found

in this work. It is important to point out that the morphology and chemical composition of the FeB/Fe₂B phase system evaluated on Armco are different and that the wear rates they determined were rated approximately from 9×10^{-4} to $4 \times 10^{-4} \text{ mm}^3/\text{Nm}$ through the coating for specific wear distances. Finally, their work never considered the individual contribution of each phase to the wear rate.

Figure 10 shows the abrasion mechanisms identified by optical profilometry on the Fe₂B phase. For both the FeB and Fe₂B phases, transition between rolling and grooving abrasion does not occur instantly, but rather there is a transition zone called mix mode abrasion zone. The increase in the concentration of abrasive causes an increase in the volume loss since the amount of abrasive particle that touches the surface of the phases of borides per unit of time is greater. If the applied load is increased and the volumetric concentration of abrasive is reduced, then the mechanism of two-body abrasion (grooving abrasion) will be predominant; in this case, the pressure between the counterpart and the abrasive increases so much that they end up acting as a single body. This mechanism is characterized by multiple grooving marks on the wear crater. The mix mode abrasion mechanism is shown in Fig. 10(c) where there are grooving marks at the center of the scar and evidence of rolling abrasion at the contour. In mix mode zone, movement of abrasive particles is held at the center of the wear scar when the contact pressure between abrasive particles and the samples increases, causing them to act as part of the counterface.

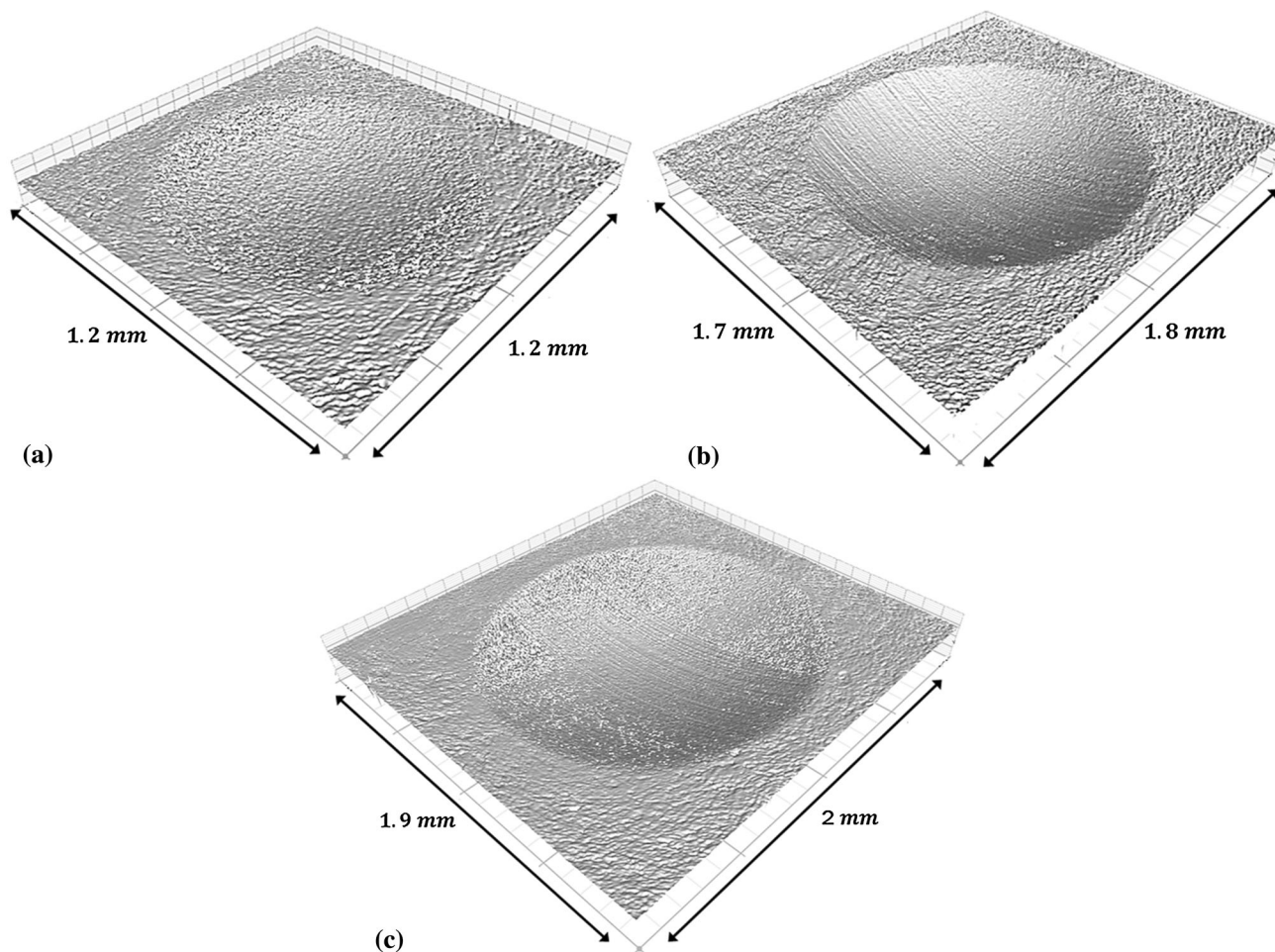


Fig. 10 Abrasion wear mechanisms identified by optical profilometry on Fe₂B phase (a) rolling abrasion 0.2 N—20%, (b) grooving abrasion 1 N—10%, (c) mix mode 1.5 N—20%

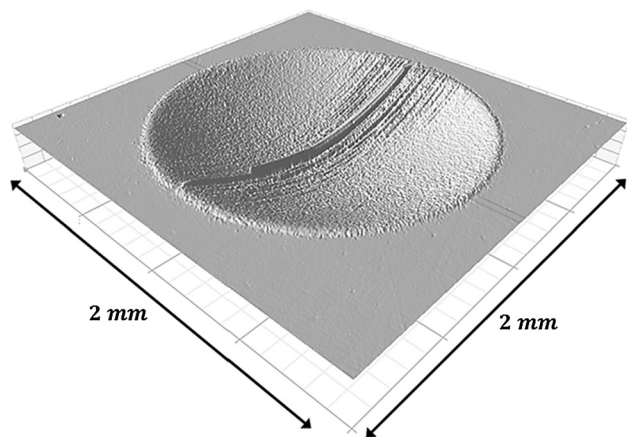


Fig. 11 Ridge's effect observed by optical profilometry

In AISI 316L steel, the Ridge's effect appears because of the low hardness and high ductility of stainless steel. The center of the wear scar was deformed when contact pressure between the sample and counterface increased avoiding flow of abrasive particle and therefore wear in this region. Ridge's effect was identified by optical profilometry in Fig. 11. According to the

results, small changes in the load and abrasive concentration can lead to transition between rolling and grooving wear in FeB and Fe₂B phases. Ductile materials (AISI 316L) have a bigger range of combinations which can result in rolling abrasion, while for harder materials this area is reduced (FeB and Fe₂B) as shown in Fig. 6 and 7.

5. Conclusions

The micro-abrasion resistance of FeB and Fe₂B phases formed on AISI 316L stainless steel and AISI 1018 steel was evaluated, respectively. In borided AISI 316L was observed a biphas FeB/Fe₂B coating; moreover, XRD patterns reveal CrB and Ni₃B. Total thickness and the FeB phase thickness are $28.18 \pm 0.53 \mu\text{m}$ and $21.72 \pm 0.95 \mu\text{m}$, respectively. A Fe₂B mono-phase coating with the presence of some FeB crystals was observed on the borided AISI 1018 low-carbon steel (total thickness of $27.4 \pm 4.25 \mu\text{m}$ and FeB phase of approximately $5 \mu\text{m}$). After diffusion annealing process was applied to the borided AISI 1018 steel, FeB crystals were dissolved. (Coating is $27.50 \pm 2.35 \mu\text{m}$.) Absence of the FeB phase on the layer is verified by the XRD pattern. The hardness and modulus of elasticity were evaluated in the coating systems by instru-

mented indentation, with the highest values in the FeB phase formed on AISI 316L (hardness = 24 GPa and $E = 350$ GPa). An increase was found in the abrasion resistance of the steel after the boriding process. Wear rates for FeB, Fe₂B, and AISI 316L stainless steel were determined by means of a bulk evaluation test on a micro-abrasion machine. The FeB phase had the highest wear abrasion resistance with a wear rate of $K_{FeB} = 7.9E^{-4}$ mm³/Nm, representing a loss of volume of 34% per newton meter applied compared with the stainless steel. The Fe₂B phase was not as resistant as the FeB phase but had a volume loss per newton meter applied of about 29% with respect to the stainless steel with a wear rate of $K_{Fe_2B} = 8.5E^{-4}$ mm³/Nm. Wear rate of AISI 316L stainless steel was calculated in $K_{316L} = 12.1E^{-4}$ mm³/Nm. According to these results, the lifetime of mechanical elements undergoing third-body abrasion wear could be increased if boriding treatment is applied to them. This is not of minor importance considering that a two-body mechanism can turn into three-body mechanism due to the formation of wear particles and the characteristics of the tribological system. Wear mode maps were constructed for FeB, Fe₂B, and AISI 316L stainless steel for a range of loads and SiC volume concentrations on the slurry. Rolling abrasion is present in all wear maps generally when applied loads are low and SiC volume concentrations on the slurry are high. Grooving abrasion was only possible on the FeB and Fe₂B phases when SiC volume concentrations decreased and applied loads increased. On the AISI 316L stainless steel, the grooving abrasion was not present and was replaced by Ridge's effect. Some wear craters in all cases showed a mixed pattern of grooving and rolling features.

Acknowledgments

This work was supported by the National Council of Science and Technology [Research Grant 183836] and the Instituto Politécnico Nacional [Research Grants 20170851 and 20170688] in Mexico.

References

1. T. Bell, Surface Engineering of Austenitic Stainless Steel, *Surf. Eng.*, 2002, **18**, p 415–422
2. Y. Kallali, A. Büyüksagis, and Y. Yalçin, Corrosion and Wear Behaviors of Boronized AISI, 316L Stainless Steel, *Met. Mater. Int.*, 2013, **19**, p 1053–1061
3. Y. Kayali, A. Büyüksagis, I. Günes, and Y. Yalçin, Investigation of Corrosion Behaviors at Different Solutions of Boronized AISI, 316L Stainless Steel, *Prot. Met. Phys. Chem. Surf.*, 2013, **49**, p 348–358
4. I. Mejía-Caballero, M. Palomar-Parvade, J. Martínez-Trinidad, M. Romero-Romo, R. Pérez Pasten-Borja, L. Lartundo-Rojas, C. López-García, and I. Campos-Silva, Corrosion Behavior of AISI, 316 L Borided and Non-Borided Steels Immersed in a Simulated Body Fluid Solution, *Surf. Coat. Technol.*, 2015, **280**, p 384–395
5. I. Campos-Silva, G. Rodríguez-Castro, in *Boriding to Improve the Mechanical Properties and Corrosion Resistance of Steel*, ed. by E. Mittemeijer, A. Somers. Thermochemical Surface Engineering of Steels, 1st ed. (Woodhead Publishing Series in Metals and Surface Engineering, UK, 2015), pp. 651–702
6. I. Campos-Silva, M. Ortiz-Domínguez, O. Bravo-Bárceñas, M.A. Doñu-Ruiz, D. Bravo-Bárceñas, C. Tapia-Quintero, and M.Y. Jiménez-Reyes, Formation and Kinetics of FeB/Fe₂B Layers and Diffusion Zone at the Surface of AISI, 316 Borided Steels, *Surf. Coat. Technol.*, 2010, **205**, p 403–412
7. M. Keddám, Simulation of the Growth Kinetics of the (FeB/Fe₂B) Bilayer Obtained on a Borided Stainless Steel, *Appl. Surf. Sci.*, 2011, **257**, p 2004–2010
8. I. Günes and I. Yildiz, Rate of Growth of Boride Layers on Stainless Steels, *Oxid. Commun.*, 2015, **38**(4A), p 2189–2198
9. Z. Nait Abdellaha, M. Keddám, and A. Elias, Modelling the Boronizing Kinetics in AISI, 316 Stainless Steel, *Acta Phys. Pol. A*, 2012, **122**(3), p 588–592
10. O. Ozdemir, M.A. Omar, M. Usta, S. Zeytin, C. Bindal, and A.H. Ucisik, An Investigation on Boriding Kinetics of AISI, 316 Stainless Steel, *Vacuum*, 2009, **83**, p 175–179
11. E. García-Bustos, M. Figueroa-Guadarrama, G. Rodríguez-Castro, O. Gómez-Vargas, E. Gallardo-Hernández, and I. Campos-Silva, The Wear Resistance of Boride Layers Measured by the Four-Ball Test, *Surf. Coat. Technol.*, 2013, **215**, p 241–246
12. M. Tabur, M. Izciler, F. Gul, and I. Karacan, Abrasive Wear Behavior of Boronized AISI, 8620 Steel, *Wear*, 2009, **266**, p 1106–1112
13. M. Ulutan, M. Yildirim, O. Elik, and S. Buytoz, Tribological Properties of Borided AISI, 4140 Steel with the Powder Pack-Boriding Method, *Tribol. Lett.*, 2010, **38**, p 231–239
14. C. Martini, G. Palombarini, G. Poli, and D. Prandstraller, Sliding and Abrasive Wear Behaviour of Boride Coatings, *Wear*, 2004, **256**, p 608–613
15. I. Günes and I. Yildiz, Investigation of Adhesion and Tribological Behavior of Borided AISI, 310 Stainless Steel, *Revista materia*, 2016, **21**, p 61–71
16. A. Günen, M. Gök, A. Erdoğan, B. Kurt, and N. Orhan, Investigation of Microabrasion Wear Behavior of Boronized Stainless Steel with Nanoboron Powders, *Tribol. T.*, 2013, **56**, p 400–409
17. G. Rodríguez-Castro, C. Reséndiz-Calderon, L. Jiménez-Tinoco, A. Meneses-Amador, E. Gallardo-Hernández, and I. Campos-Silva, Micro-Abrasive Wear Resistance of CoB/Co₂B Coatings Formed in CoCrMo Alloy, *Surf. Coat. Technol.*, 2015, **284**, p 258–263
18. K. Adachi and I. Hutchings, Sensitivity of wear rates in the micro-scale abrasion test to test conditions and material hardness, *Wear*, 2005, **258**, p 318–321
19. R. Trezona, D. Allsopp, and I. Hutchings, Transitions between two-body and three-body abrasive wear: influence of test conditions in the microscale abrasive wear test, *Wear*, 1999, **225–229**, p 205–214
20. K. Bose and R. Wood, Optimum tests conditions for attaining uniform rolling abrasion in ball cratering tests on hard coatings, *Wear*, 2005, **258**, p 322–332
21. M. Gee, A. Gant, I. Hutchings, R. Bethke, K. Schiffman, K. Van Acker, S. Poulat, Y. Gachon, and J. von Stebut, Progress towards standardization of ball cratering, *Wear*, 2003, **255**, p 1–13
22. M. Gee, A.J. Gant, I.M. Hutchings, Y. Kusano, K. Schiffman, K. Van Acker, S. Poulat, Y. Gachon, J. von Stebut, P. Hatto, and G. Plint, Results from an interlaboratory exercise to validate the micro-scale abrasion test, *Wear*, 2005, **259**, p 27–35
23. I. Campos-Silva, M. Flores-Jiménez, G. Rodríguez-Castro, E. Hernández-Sánchez, J. Martínez-Trinidad, and R. Tadeo-Rosas, Improved fracture toughness of boride coating developed with a diffusion annealing process, *Surf. Coat. Technol.*, 2013, **237**, p 429–439
24. International Organization for Standardization – ISO. ISO 14577-1: metallic materials: instrumented indentation test for hardness and materials parameters. Part 1: test method. Geneva: ISO; 2002
25. W.C. Oliver and G.M. Pharr, An improved technique for determining hardness and elastic modulus using load and displacement sensing indentation experiments, *J. Mater. Res.*, 1992, **7**, p 1564–1583
26. I.E. Campos-Silva and G.A. Rodríguez-Castro, Boriding to Improve the Mechanical Properties and Corrosion Resistance of Steels, *Thermochemical Surface Engineering of Steels*, 1st ed., E.J. Mittemeijer and M.A.J. Somers, Ed., Woodhead-Elsevier Publishing, Cambridge, 2015, p 658–661
27. C. Badini, C. Gianoglio, and G. Pradelli, Distribution of Chromium and Nickel Between the Phases Present in the Borided Layer of Alloy Steels, *Metall. Sci. Technol.*, 1985, **3**, p 10–15
28. J. Rus, C.L. Leal, and D.N. Tsiapas, Boronizing of 304 Steel, *J. Mater. Sci. Lett.*, 1985, **4**(5), p 658–661
29. C. Martini, G. Palombarini, and M. Carbucchio, Mechanism of Thermochemical Growth of Iron Borides on Iron, *J. Mater. Sci.*, 2004, **39**(3), p 933–937